

## A Study of Two-Dimensional Dry Convective Plume Modes with Variable Critical Level Height

MICHAEL T. KIEFER

*Department of Marine, Earth, and Atmospheric Sciences, North Carolina State University, Raleigh, North Carolina*

YUH-LANG LIN

*Cary, North Carolina*

JOSEPH J. CHARNEY

*Northern Research Station, USDA Forest Service, East Lansing, Michigan*

(Manuscript received 25 September 2006, in final form 19 March 2007)

### ABSTRACT

This study investigates the impact of wind speed and critical level height on dry convection above a prescribed heat source. This is done using the Advanced Regional Prediction System (ARPS) model in its two-dimensional form with an imposed 400-K soil potential temperature perturbation. The result of these experiments is the identification of three modes of convective plumes. The first, termed multicell convective plumes, is analogous to multicell convection generated from squall-line cold pools in the moist atmosphere. The second mode, a deep wave mode, consists of disturbances with wavelengths of 7–10 km and results from the multicell plumes perturbing the dynamically unstable shear flow centered at the critical level. The third mode, termed the intense fire plume, has stronger updrafts than the multicell mode and is marked by quasi-stationary movement and substantial low-level inflow and upper-level outflow. The presence of a critical level is shown to be crucial to the development of both the deep wave and intense plume modes. The intense fire plume mode is most consistent with the so-called fire storm, or conflagration phenomenon, in which strong updrafts and low-level indrafts can produce mesocyclones and tornadic fire whirls capable of significant damage. This study marks an important step in understanding the dynamics behind the fire storm phenomenon, as well as other types of convection (multicell and deep wave) that may be generated by a fire.

### 1. Introduction

Forest fires have a profound impact on atmospheric circulations primarily due to the large temperature anomalies produced by a fire. Anomalies of 40–60 K, in combination with the substantial amounts of moisture produced during the combustion process, can produce dramatic buoyancy-driven horizontal and vertical circulations that feed back on the fires via mechanisms, including the advection of hot gases and burning material, and the mixing of air with flames to increase flame temperatures, thereby increasing combustibility (Jenkins et al. 2001). Early numerical modeling studies of plumes above forest fires considered only the temporally averaged plume characteristics, the result of which

was the classification of “plume-dominated” and “wind-dominated” fires, with weaker (stronger) mean winds and greater (lesser) heat output associated with the former (latter; Byram 1966; Grishin et al. 1984). Plume-dominated fires featured more upright plumes while wind-dominated fires were associated with plumes strongly tilted downstream.

However, the complex nonlinear processes associated with fires can lead to a transition from small, relatively easily managed fires into multicell fire plumes and even intense fire plumes capable of strong mesocyclonic rotation with scales as large as 400 m in the horizontal and several kilometers in the vertical. The fundamental dynamics of this process are still not well understood. The multicell plume structure consists of a series of discrete vertical protrusions of soot and smoke with a substantial lateral component of motion, while the intense fire plume mode consists of one large, generally upright plume with a strong updraft. Examples of these two phenomena include lidar observations in

---

*Corresponding author address:* Michael Kiefer, Department of Marine, Earth, and Atmospheric Sciences, North Carolina State University, Raleigh, NC 27695-8208.  
Email: mtkiefer@ncsu.edu

Banta et al. (1992, see their Figs. 4 and 8) and numerical simulations using a coupled fire–atmosphere model in Clark et al. (1996, see their Fig. 9). In this study, we are interested in the characteristics and dynamics of these temporally varying phenomena.

Multicellular convection is a phenomenon that has been studied in depth through both observations and modeling for more than thirty years [see brief reviews in Lin et al. (1998, hereafter LDK) and Fovell and Tan (1998)]. The classic model of multicell convection involves a cold pool, resulting from preexisting squall-line convection, propagating outward, with the resulting low-level convergence providing a nearly steady-state updraft with which discrete cells periodically separate and move from front to rear (with respect to the motion of the cold pool). Care must be taken in applying any moist convective multicell mechanism to the particular problem in this study, dry convection in a shear flow with a critical level; two phenomena that appear similar need not be produced by similar means.

McRae and Stocks (1987) and McRae and Flannigan (1990) describe fire-driven circulations strong enough to rip out standing trees and remove surface organic material, exposing bare mineral soil underneath. Several examples of such intense fire plume phenomena, also referred to as conflagrations, are present in the available literature. Church et al. (1980) simulated a large vortex with an embedded ropelike funnel (see their Fig. 6) in an experiment involving a 105 fuel oil burner array known as the Meteotron. While the funnel was only approximately 5 m in diameter, it is apparent from the photograph and the description in their text that a much broader scale rotating plume existed above the funnel. Simard et al. (1983) describe firefighter observations of what they concluded were horizontal roll vortices that locally perturbed the wind field and produced intense downdrafts at an early stage of the Mack Lake fire in northern Lower Michigan during May 1980. The unpredictable movement of the fire and lofting of firebrands (burning material) igniting new fires led to the loss of life of a firefighter suddenly caught between two fires. Additionally, McRae and Flannigan (1990) detail 20 occurrences of vertical vortices, some of which grew to 400 m in diameter existing for as long as 2 h before dissipating, during a 5-yr period of prescribed fires in Ontario, Canada.

Observations indicate that the environmental wind field occasionally exhibits a critical level during such extreme phenomena. A critical level is defined as a level of the atmosphere where the propagation speed ( $c$ ) of a wave or disturbance equals the mean wind speed ( $U$ ) (e.g., LeBlond and Mysak 1978). As a simple example, where thermal forcing is fixed, a level of the

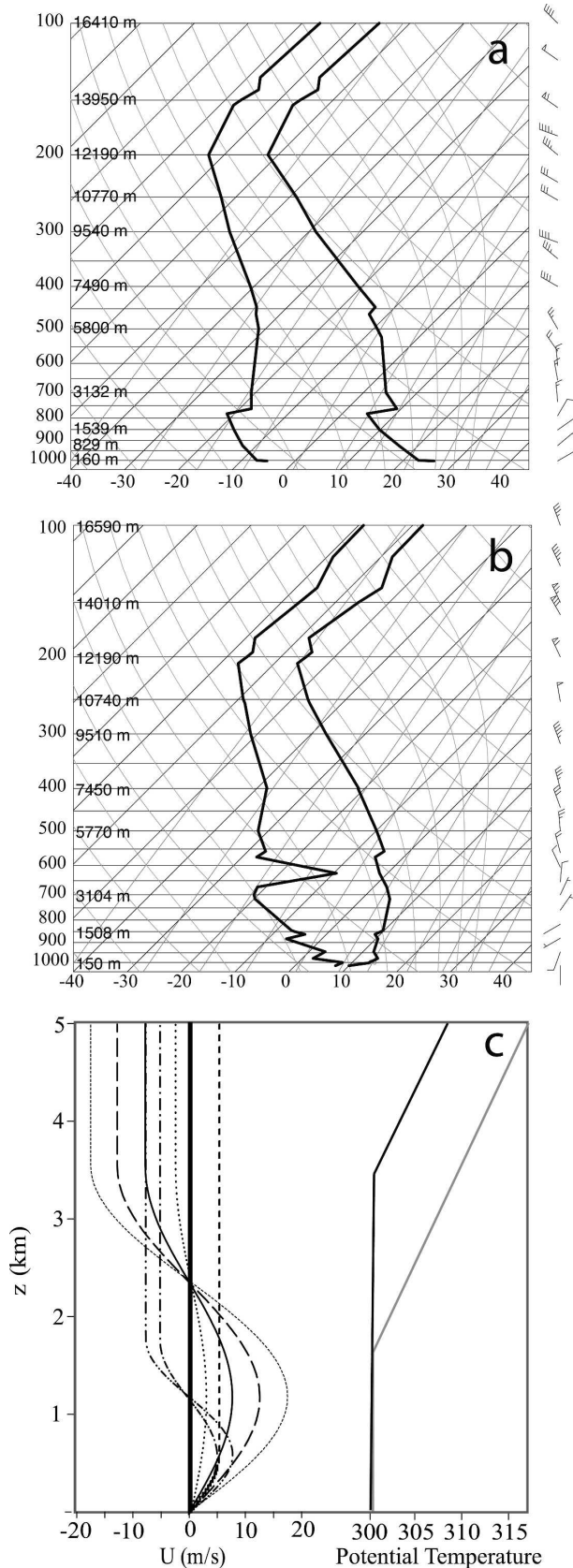
atmosphere where the basic wind speed equals zero represents a critical level. In the special case of steady-state flow with fixed forcing, a wind reversal level is a critical level. As illustrated by the 0000 UTC 22 October 1996 San Diego, California, sounding (Fig. 1a) during a typical Santa Ana wind-driven conflagration (Raphael 2003), wind reversal levels were present. While the observed sounding did not feature a zero mean wind level, the expectation that a large fire in the real world is not fixed but rather propagates at speeds on the order of  $1 \text{ m s}^{-1}$  (Jenkins et al. 2001) indicates that a critical level might well exist in such an environment. As a second example, one of the prescribed fires described by McRae and Flannigan that produced a large, intense vortex, that is, the Horwood fire near Foleyet, Ontario, Canada, with a diameter of 200 m, developed in an environment with a critical level, as seen in the 1200 UTC 1 August 1987 Moosonee, Ontario, sounding (Fig. 1b). Additionally, the vortex observed in Church et al. (1980) described above occurred in an environment with a wind reversal layer and near-adiabatic lower atmosphere (see their Fig. 7). The limited number of studies on this phenomenon and the low density of upper-air observing sites limit this assessment. *Contrary to the multicell plume, we hypothesize that for a fire of moderate intensity, the intense fire plume cannot be produced by advection alone; it is instead produced in an environment with a critical level.*

This paper is organized as follows. In section 2, a description of the model utilized in this study as well as the experiment design will be presented. Section 3 is divided into five sections and will present results consisting of (section 3a) multicell convective plumes, (section 3b) cell splitting and merging, (section 3c) deep trapped waves, and (section 3d) intense convective plumes. As part of testing our hypothesis, cases with predominantly multicellular fire-induced convective circulations will be evaluated before considering cases in which a transition to an intense fire plume mode more consistent with observed conflagrations occurred. The critical level hypothesis for the development of conflagrations will then be proven by numerical experiments in hopes of providing a possible mechanism for the extreme phenomenon. Section 3e considers sensitivity of the results presented to experiment details at the lower boundary, namely, surface fluxes and heating structure. Finally, section 4 will summarize the results presented and outline future work.

## 2. Model description and experiment design

### a. Model description

The numerical model utilized for this study is the Advanced Regional Prediction System (ARPS) version 5.1.0



(Xue et al. 2000, 2003). ARPS is a three-dimensional, compressible, nonhydrostatic cloud model, which is integrated on a staggered grid with terrain-following coordinates. The model has a vertical coordinate that may be stretched to increase low-level resolution. Open lateral boundaries are utilized to allow disturbances to exit the computational domain. For our simulations, ARPS has been initialized with a single vertical profile of temperature, moisture, and wind velocity, although the model does have the option of initializing with a three-dimensional dataset. The upper boundary condition for all simulations is a sponge layer beginning at 6.1 km above the surface and extending up to the top boundary at 10 km. The sponge layer is constructed using a Rayleigh friction, which has a coefficient defined as  $\nu(z) = (\nu_t/2)\{1 - \cos[\pi(z - z_1)/(z_t - z_1)]\}$  in the sponge layer, where  $z_1$  is the height of the bottom of the sponge layer (in this case 6.1 km),  $z_t$  is the top of the domain, and  $\nu_t$  is the maximum Rayleigh friction coefficient, set to  $0.003 \text{ s}^{-1}$  for this study.

A 1.5-order turbulent kinetic energy (TKE) subgrid-scale turbulence closure scheme is utilized, in addition to a simplified surface radiation physics scheme (see Xue et al. 2000, 2001 for details). The model is initialized with a dry atmosphere, and as such no microphysics scheme is necessary. A surface physics parameterization scheme based on bulk drag/heat transfer relations was utilized, where the surface drag and heat flux are expressed as  $\tau_0 = \bar{\rho} C_d U^2$  and  $H_0 = \bar{\rho} C_h U(\theta - \theta_g)$ , respectively (Xue et al. 2001). Here  $\theta$  refers to the potential temperature at the lowest model level and  $\theta_g$  is the specified potential temperature at ground level, and  $U$  is the mean wind at the lowest model level. Both momentum drag ( $C_d$ ) and heat transfer ( $C_h$ ) coefficients were set to a constant value of  $3 \times 10^{-3}$  and a basic-state ground potential temperature of  $\Theta_0 = 295 \text{ K}$  was assumed. Details on the sensitivity of the results of this study to the surface physics are presented in section 3e. Additionally, the Coriolis force was neglected in these simulations as it has a negligible impact on the short-lived convection of the type considered in this study. Fourth-order finite differencing of the advection terms is used in both the vertical and horizontal for numerical accuracy.

←

FIG. 1. Observed soundings of temperature, dewpoint, and wind from (a) San Diego, CA, 0000 UTC 22 Oct 1996 and (b) Moosonee, ON, 1200 UTC 1 Aug 1987; and (c) model profiles of wind speed for MID7.5 (solid), MID12.5 (long dash), MID17.5 (short dash), MID2.5 (dot), LOW5 (dot-dash), LOW7.5 (dot-dot-dash), and NOCL5 (medium dash) cases, and potential temperature for MID cases (black) and LOW cases (gray). See text for details.

### b. Experiment design

A two-dimensional computational domain is utilized with uniform horizontal grid spacing of 50 m in the horizontal and 40 m in the vertical. The model domain was chosen to be 40 km in the  $x$  direction and 10 km in the  $z$  direction. With a domain of 40 km and Orlanski-type open lateral boundary conditions, wave reflections from lateral boundaries have been minimized. Simulations were also performed with a three-dimensional domain, with uniform horizontal grid spacing of 100 m in the horizontal and a stretched vertical grid with spacing varying from 40 m in the surface layer to about 150 m at the base of the Rayleigh sponge layer. The model domain was chosen to be 60 km in the  $x$  direction and 10 km in the  $z$  direction. Details of the three-dimensional experiments will be discussed in section 3d to evaluate the role of the critical level in the development of a fully three-dimensional buoyant plume.

The basic temperature and wind profiles used to initialize ARPS are presented in Fig. 1c. As mentioned previously, all simulations performed for this study were initialized with no moisture, as this is a study of purely dry convection. All cases feature a westerly jet in the lower portion of the domain with a wind reversal and constant easterly flow in the upper part of the domain. The exception to this is a special case run without a critical level (NOCL5, see medium dashed profile in Fig. 1c). This case will be compared to an experiment with the same wind speed amplitude but with a critical level in the basic state (LOW5, see dot-dot-dash profile in Fig. 1c) to consider the impact of a critical level on the plume mode.

The deep neutral layer coincident with the variable shear layer in the ARPS sounding is consistent with an environment conducive to fire development (Werth and Ochoa 1993). The correspondence between mixed layer depth and critical level height apparent in Fig. 1c was determined from a review of Santa Ana wind events in Southern California. While this study focuses on sensitivity of dry convection to critical level height and basic wind speed, additional experiments indicate that the main impact of the mixed layer depth is to control the depth of convection in the intense plume mode (not shown). The maximum height of the intense plume mode to be discussed later might be greater given a deeper mixed layer. Three sets of cases were performed, with critical level heights of 1.2 (LOW cases), 2.3 (MID cases), and 4.6 km (HIGH cases). Within each case, wind speeds were varied to evaluate the impact of wind speeds above and below the critical level on cell behavior. Seven simulations will be considered in this paper, LOW5, LOW7.5, MID2.5,

TABLE 1. Summary of experiments. Convection is initiated in the model by placing a 400-K soil potential temperature perturbation in the center of the  $x$  domain. The radius of the perturbation is 260 m, and the perturbation is fixed throughout the simulations.

Case	Critical level height (km)	Max low-level wind speeds ( $\text{m s}^{-1}$ )	Neutral layer depth (km)
NOCL5	—	5	1.8
LOW5	1.2	5	1.8
LOW7.5	1.2	7.5	1.8
MID2.5	2.3	2.5	3.6
MID5*	2.3	5	3.6
MID7.5	2.3	7.5	3.6
MID12.5	2.3	12.5	3.6
MID17.5	2.3	17.5	3.6
HIGH5*	4.6	5	5.4
HIGH7.5*	4.6	7.5	5.4

\* Experiments not shown.

MID7.5, MID12.5, MID17.5, and the NOCL5 case (Fig. 1c). Results from the HIGH critical level cases were found to be very similar to those from the MID cases and will not be presented here. Convection is initiated in the model by placing a 400-K soil potential temperature perturbation in the center of the  $x$  domain. The radius of the perturbation is 260 m and the perturbation is fixed throughout the simulations. See Table 1 for a summary of experiments performed.

## 3. Results and discussion

### a. Multicell convective plume mode

The primary result of the six cases performed was the discovery of three distinct modes of convection. Figure 2 presents Hovmöller (time-space) diagrams at the 600-m level for cases NOCL5 and MID7.5 that exhibited multicell plume behavior. For the NOCL5 case (Fig. 2a), individual cells develop above the hotspot and then propagate downstream. Updraft speeds generally do not exceed  $6 \text{ m s}^{-1}$  and are strongest near the hotspot. In addition to the downstream propagating convective cells, there is a series of stationary convective cells that developed at the downstream side of the prescribed fire. Figure 2b indicates that the MID7.5 case exhibits a similar plume behavior, especially before  $t = 80$  min (see section 3b for discussion about behavior after 80 min). In Fig. 3, a plot of NOCL5 vertical velocity and potential temperature in the  $x$ - $z$  plane 40–75 min after initialization, it is seen that discrete cells propagate downstream (see dashed line tracing path of one particular cell) at about  $5 \text{ m s}^{-1}$ , transporting weakly heated air from the hotspot eastward.

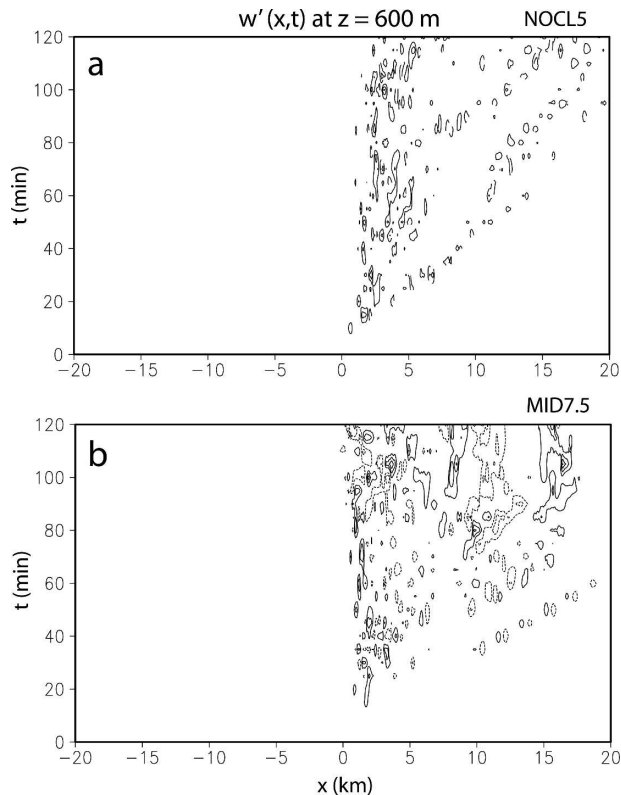


FIG. 2. Hovmöller (time–space) diagrams of vertical velocity at  $z = 600$  m for multicell fire plume cases (a) NOCL and (b) MID7.5. Contour interval is  $2 \text{ m s}^{-1}$ . Hotspot located at  $x = 0$ .

Comparison of Fig. 3 with Fig. 4, identical to Fig. 3 but for the MID7.5 case, indicates that as expected from the Hovmöller diagram, discrete multicell plumes are present. The NOCL5 case will be further discussed in section 3c in an evaluation of critical level impacts on the intense plume mode development.

What is readily apparent from a comparison of Fig. 4 with a similar plot in LDK after onset of quasi-steady oscillatory behavior (see vertical velocity contours in their Fig. 2) is the qualitative similarity of cell structure. Despite the differences in the scales of the simulated convection (the breadth of cells in LDK is about one order of magnitude larger than that noted for cells in this study), similarities do exist. Cell aspect ratios, defined as the ratio of horizontal wavelength to cell depth, are roughly 1:1 in the vicinity of the forcing for both LDK's multicell convection and that simulated in this study. It should be noted that the upstream tilting of cells above about 9 km in LDK's figure is due to the presence of vertically propagating gravity waves above the tropopause. The lack of cell tilt in Fig. 4 is reasonable given that all cells in this case remained at or below the interface between the neutral and stable layers (at about 3.5 km AGL).

One important characteristic to be considered is the origin of the multicells. LDK as well as Yang and Houze (1995) attributed cell behavior downstream of the cell origin to the fact that the cells were vertically trapped gravity waves. As the base-state atmosphere in these experiments is nearly statically neutral, the multicell convection in this case cannot be an internal gravity wave phenomenon. Instead, the cells in this case are more akin to buoyant pulses of air (i.e., thermals) that ascend and are advected downstream by the background flow. This argument is applicable to fire plumes in both two- and three-dimensional flows, whereas alternative arguments involving vertical vorticity, such as buoyant cells forming via shear instability on the upwind side of a plume (Cunningham et al. 2005), is not relevant in a two-dimensional framework such as this.

#### b. Cell splitting and merging

Multicell storm studies of Fovell and Dailey (1995), LDK, and Lin and Joyce (2001) have simulated two interesting phenomena: cell splitting and merging. Lin and Joyce (2001) evaluated simulations from Fovell and Dailey, in addition to their own simulations, for instances of cell splitting/merging. As Lin and Joyce point out, little research has been done to investigate the causes of these phenomena. When one considers the very real impact fire-driven circulations can have on fire behavior (Jenkins et al. 2001), the need for an understanding of cell behavior in this study becomes more apparent. Figure 5, a five-panel  $x$ – $z$  plot of vertical velocity every five minutes beginning at 40 min ( $t + 0$ ), indicates examples of cell splitting as well as cell merging. Cell M3 is an excellent example of a discrete cell that undergoes cell splitting. Cell M3 is initially located 2 km downstream of the hotspot ( $x = 0$ ) at  $t + 0$  and moves approximately  $5 \text{ m s}^{-1}$  eastward to a position near  $x = 6$  km at  $t + 15$ , before appearing to split into two centers near  $x = 7.5$  km 5 min later. A similar cell split takes place earlier in the simulation, between 25 and 30 min following initialization (not shown). Both cell separations occur between 6 and 8 km downstream of the hotspot, in contrast to simulations by Lin and Joyce (2001) and Fovell and Dailey (1995) in which division of the cells occurred when the cell updraft had reached its greatest magnitude. That tended to occur close to the gust front updraft, when cells were in the growing mode. In this study, in the absence of anything resembling a gust front updraft, the type of cell splitting previously observed is not relevant. What is noticeable is as cell M3 approaches the position at  $t + 15$  where it begins to split, the upper part of the cell tilts upstream, consistent with differential advection (see wind profile

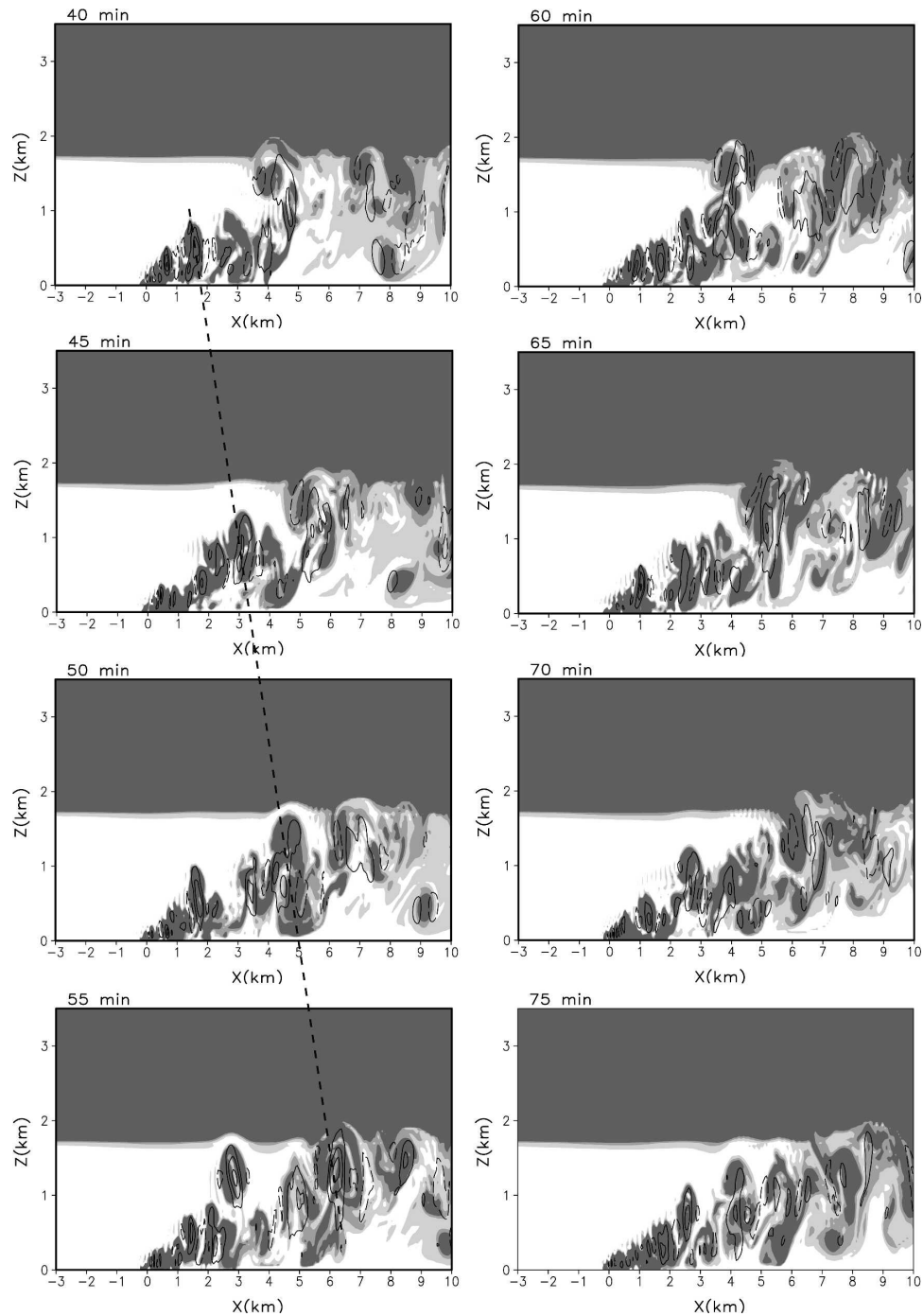


FIG. 3. Vertical cross sections of vertical velocity (thin contours with  $2 \text{ m s}^{-1}$  intervals) and potential temperature (shaded) for a portion of the computational domain for the NOCL5 case. Potential temperature values greater than  $300.1 \text{ K}$  are shaded light ( $300.1\text{--}300.2 \text{ K}$ ), medium ( $300.2\text{--}300.3 \text{ K}$ ), and dark ( $>300.3 \text{ K}$ ). Positive (negative) values of vertical velocity are solid (dashed). The corresponding integration time is shown at the top of each panel. See text for description of cell traced by dashed line.

in Fig. 1c) by the basic wind tilting the cell and pulling it into two separate centers. The lower portion of cell M3, near  $x = 6 \text{ km}$  at  $t + 15$ , is located at the level of the maximum wind speed and is advected to near  $x = 8 \text{ km}$ ,

while the upper portion, at the elevation of the critical level, lags behind. This appears to be the mechanism for cell separation for the multicell convection in this case.

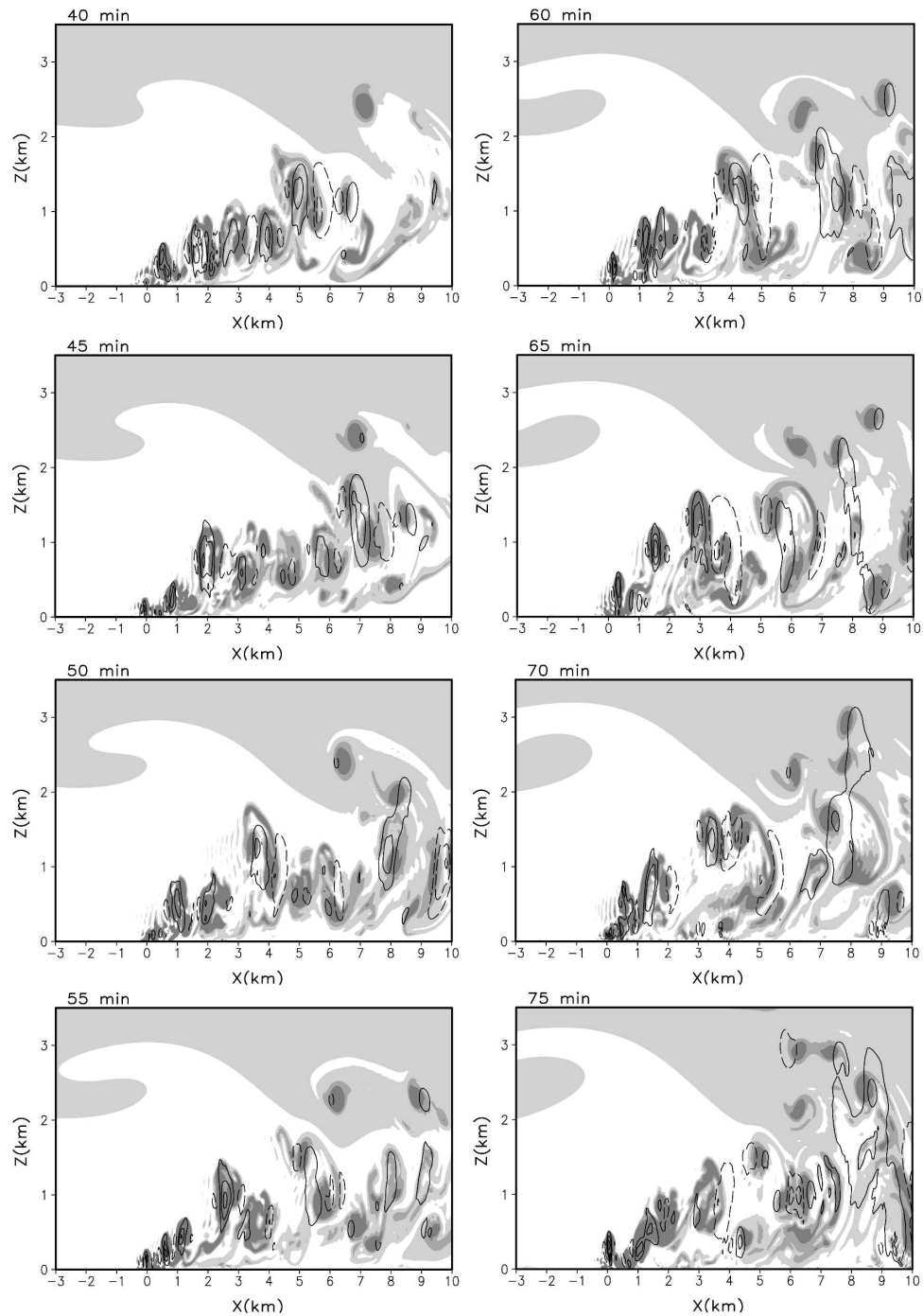


FIG. 4. As in Fig. 3 but for the MID7.5 case.

The second phenomenon noted, cell merging, has also been described in Lin and Joyce (2001). This phenomenon occurs twice during the 20-min period evaluated in Fig. 5, the first taking place between  $t + 5$  and  $t + 10$  involving cells M0 and M1. Cells M0 and M1, positioned near  $x = 5$  and  $6$  km, respectively, at  $t + 0$ , each propagate approximately  $1.5$  km by  $t + 5$ , with M1

weakening and M0 retaining its strength and expanding vertically. At  $t + 10$ , it is apparent that the two cells have become linked, with cell M1 strengthening and M0 having weakened (M0 has no closed contour at  $t + 10$  and is located near  $z = 2.5$  km). By  $t + 15$ , the cells have separated and cell M1 is located near  $x = 9$  km, with M0 having shifted out of the figure. The

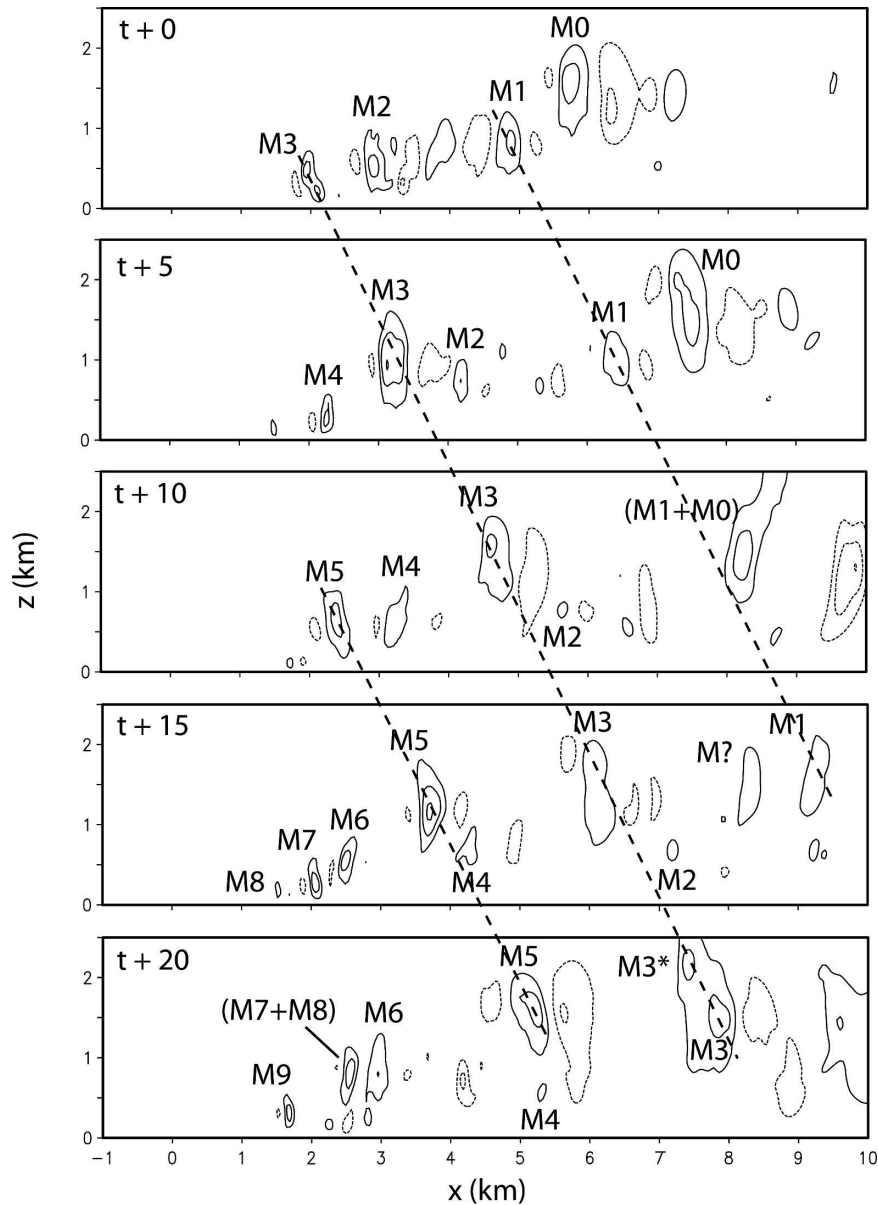


FIG. 5. Vertical cross sections of vertical velocity for the MID7.5 case, beginning at  $t = 40$  min. The contour interval of all panels is  $2 \text{ m s}^{-1}$ . Cells have been labeled M0–M9; dashed lines trace the evolution of cells M1, M3, and M5.

second example of cell merging takes place between  $t + 15$  and  $t + 20$  involving cells M7 and M8. A reasonable question to ask is why cell M3 at  $t + 15$ , located at about the same level as M0 10 min earlier, splits into two cells while cell M0 does not split but instead merges briefly with cell M1. What may distinguish a cell that will split into two centers (M3, e.g.) from a cell that will not (M0) is the proximity of a cell of equal or lesser intensity. Two kilometers separated the closest cell from cell M3, while only a 1-km distance existed between cells M1 and M0. M0 could not escape the influ-

ence of cell M1 following closely behind, while cell M3, a lone cell, was able to undergo the splitting process uninterrupted.

### c. Deep wave mode

Due to the importance of advection in the behavior of squall-line multicell convection and the analogous multicell plumes in the MID7.5 case, a second case was considered with stronger wind speeds in the layer below (and above) the critical level. Cell behavior for the MID12.5 and MID17.5 cases was found to be notice-

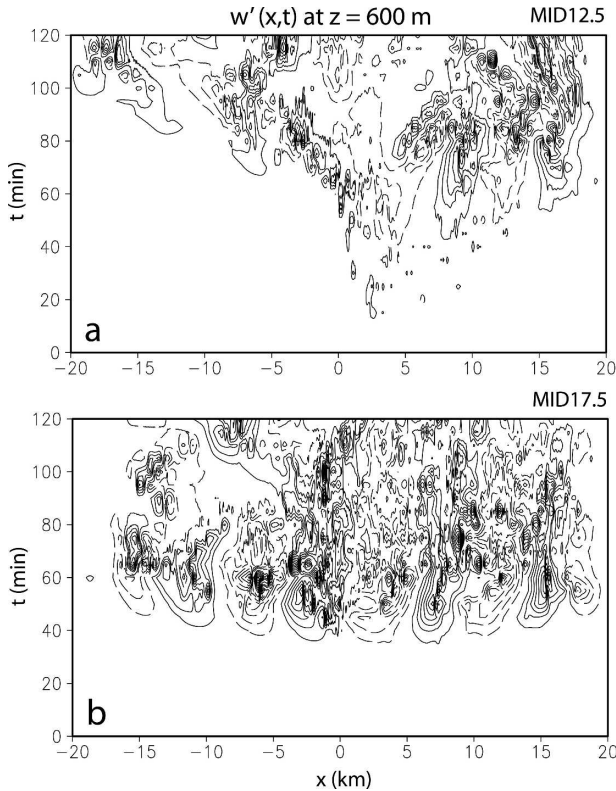


FIG. 6. As in Fig. 2 but for the deep wave cases, (a) MID12.5 and (b) MID17.5.

ably different in nature than that of MID7.5, although important similarities are present as well. Figure 6 shows the Hovmöller diagrams of vertical velocity at  $z = 600$  m for cases MID12.5 and MID17.5, which indicate nearly stationary alternating updrafts and downdrafts with large wavelengths of 7–10 km. Individual small discrete cells can be discerned in the MID12.5 case, while the long wavelength mode obscures any such activity in the MID17.5 case. Details of these cases will be addressed below, including the chaotic nature of the convection beyond about 70 min in the MID17.5 case and the westward drift of growing cells near the hotspot in the MID12.5 case.

Figure 7 reveals for the MID12.5 case that while cells within a few kilometers of the hotspot exhibit multicell behavior as in the MID7.5 case (propagating about  $3\text{--}4$  m  $\text{s}^{-1}$  downstream), intense larger-scale disturbances that develop beyond about 3 km downstream of the hotspot constitute an apparent departure from the previously analyzed case. In actuality, these phenomena were also apparent in the MID7.5 time–space plot after about 80 min, with wavelengths of about 7 km common to both cases (see Fig. 2b). One impact of this mode is the transport of higher potential temperature air originating in the stratified layer above 4 km into the neutral

layer. Heated air within a few kilometers of the hotspot is also noted in Fig. 7.

Figure 8, a plot of vertical velocity at  $t = 40$  min as in Fig. 7 except with the entire  $x$  domain east of the hotspot displayed, illustrates a phenomenon similar to one investigated in a numerical modeling study by Redelsperger and Clark (1990), wherein boundary layer eddies were found to develop within a shear layer over a gently sloping heated surface, with the eddies acting as barriers to the background wind flow. The result was the development of deep internal gravity waves with horizontal scales of 11 km and linkages to the boundary layer eddies similar in appearance to the phenomenon in Fig. 8 (cf. Fig. 4 in Redelsperger and Clark 1990).

Given the basic-state neutral lower atmosphere and the critical level in the basic wind profile in this study, a different explanation is in order. The development of the deep wave mode can in fact be attributed to the perturbing of the flow near the critical level, where strong shear instability exists, by the plumes developing above the hotspot. The result of this is the development of Kelvin–Helmholtz waves (Stull 1988; LeBlond and Mysak 1978). One can deduce the strong shear instability from the layer of strong shear and very weak stable stratification in Fig. 1c. An estimation of the bulk Richardson number,

$$\text{Ri}_b = \frac{g\Delta\bar{\theta}\Delta z}{\theta(\Delta\bar{U})^2}, \quad (1)$$

near the critical level (i.e., the wind reversal layer) yields a value of 0.01, satisfying the  $0 \leq \text{Ri}_b < 0.25$  requirement for shear instability (Lindzen and Rosenthal 1983). The unstable growth of the flow perturbation can be seen in Figs. 9a and 9b, where between 25 and 45 min, a small region of overturning near  $(x, z) = (+3, 2.5)$  km becomes more pronounced with time, with the “cat’s eye” or braided rope appearance at  $t = 25$  min evolving into a series of vortices by  $t = 45$  min. By this later time upshear-tilted waves have become apparent in the stably stratified fluid above about 3 km, while evanescent waves with no phase tilt have formed in the near-neutral lowest 2 km, consistent with energy arguments discussed by Lin and Chun (1993) for dynamically unstable shear flows.

A rather peculiar deviation from the MID7.5 cell behavior is the westward progression of the cell origin point during the 35-min period shown in Fig. 7, from near  $x = 0$  at  $t = 40$  to near  $x = -1.5$  km at  $t = 75$  min (also see Fig. 6a). This appears to reflect a subcritical near-surface momentum forcing regime analogous to the subcritical density current regime described in Ray-

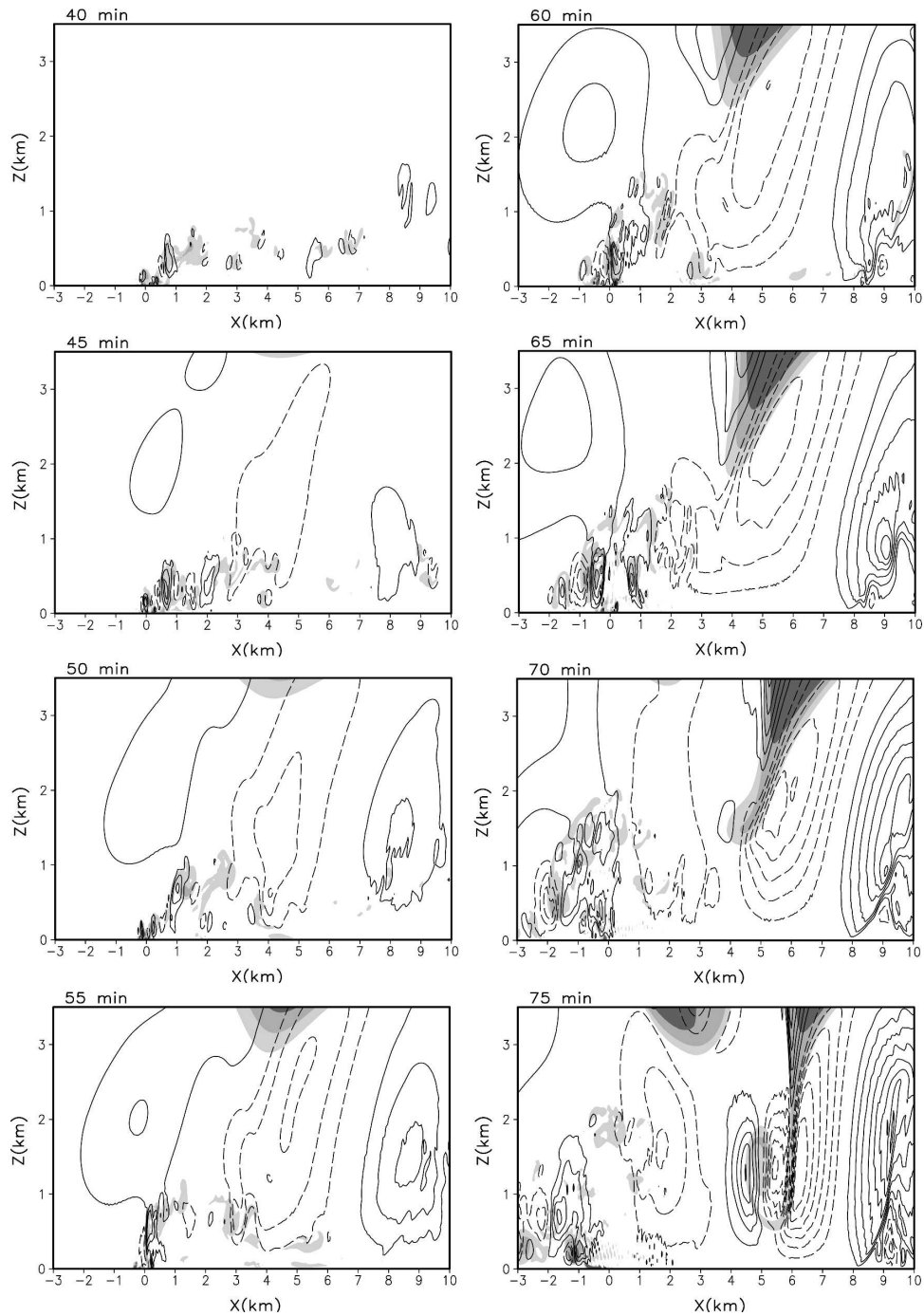


FIG. 7. As in Fig. 3 but for the MID12.5 case, with potential temperature values greater than 300.5 K shaded light (300.5–301.5 K), medium (301.5–302.5 K), and dark ( $>302.5$  K).

mond and Rotunno (1989) and Lin et al. (1993), where a region of reversed flow is able to propagate against the basic wind. Such a region of reversed flow can be seen in Fig. 10 below 500 m, between  $-3$  and  $+3$  km. At first glance, the physical reasoning for this development appears to be the increasingly intense downward

branch of one of the deep waves. Figure 10, an  $x$ - $z$  plot below 2 km at  $t = 60$  min, illustrates an easterly low-level jet with wind speeds of  $8$ – $10$   $\text{m s}^{-1}$  below 250 m, the apparent result of the strong downward motion near  $x = 4.5$  km. Further analysis reveals that the strong curvature of the streamlines away from the surface

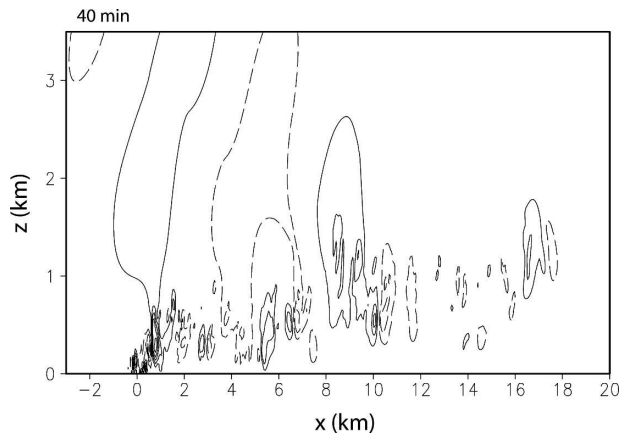


FIG. 8. As in Fig. 7 but for  $t = 40$  min with entire domain east of the hotspot displayed. Note contour interval has been increased to  $1 \text{ m s}^{-1}$ .

due to the strengthening vortex induces a westward-directed pressure gradient force below and downstream of the vortex base (see thick arrow in Fig. 10) and subsequent development of a region of reversed flow, indicative of boundary layer separation. Convergence between the low-level basic wind and the near-surface easterly flow supports the development of the multicell

convection that is then advected eastward by the basic wind. The cells in Fig. 7 progress at most about 3 km to the east before dissipating in the vicinity of the downward branch of the westernmost large wave.

For comparison to the MID12.5 case, a second simulation with a higher mean wind speed, MID17.5, was performed (Fig. 6b). Considering the stronger mean wind speeds and hence the greater amount of energy in the background flow, the dominance of the strong deep wave modes is quite reasonable. It can be discerned from Fig. 6b that the onset of the deep wave mode is earlier than in the MID12.5 case, and that the long wavelength mode obscures any multicell activity near the hotspot. From Figs. 9c and 9d, it is apparent that the critical level vortices develop earlier and become more intense than in the MID12.5 case, as do the associated deep waves. Figure 11, as in Fig. 7 but for the MID17.5 case, indicates that the multicell mode does exist, but the cells are thin and fairly weak. The tendency for the position of new cell development to drift west from the hotspot is also noted in Fig. 11 (cf.  $t = 40\text{--}50$  min), although this was not apparent from Fig. 6. Figure 11 also illustrates the transport of heated air westward away from the hotspot as a result of the reversed flow.

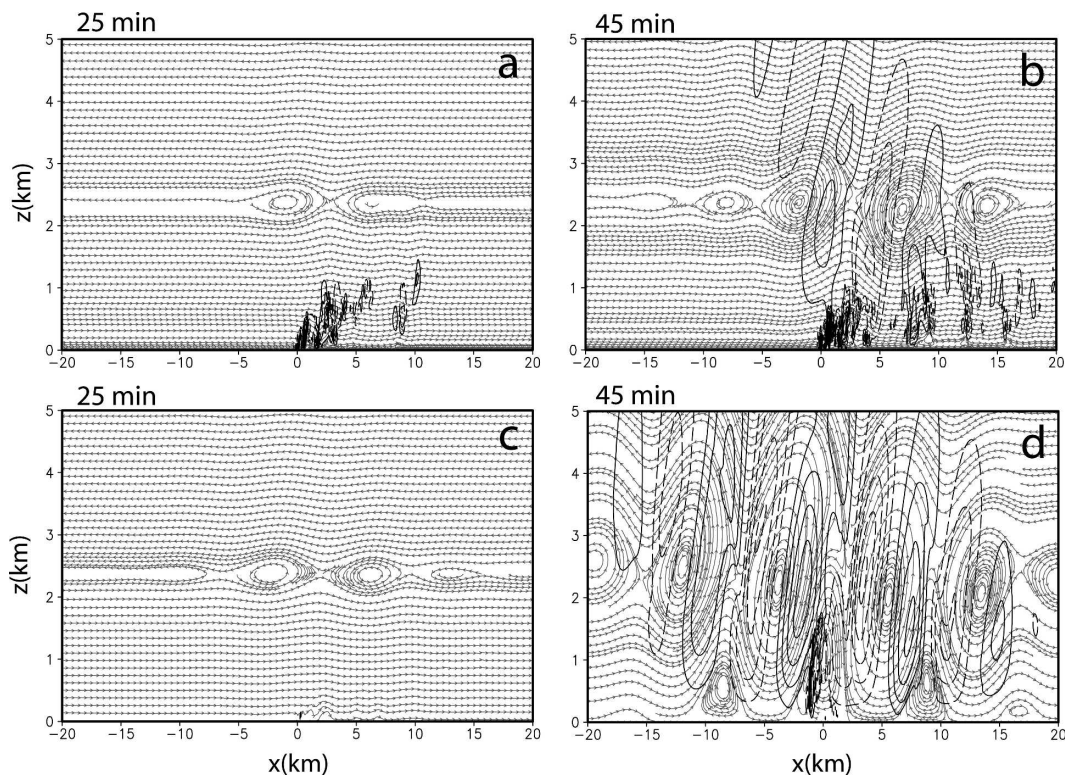


FIG. 9. Streamlines at (left)  $t = 25$  min and (right)  $t = 45$  min for (a), (b) MID12.5 and (c), (d) MID17.5 cases, with vertical velocity overlaid. Contour interval is  $2 \text{ m s}^{-1}$  for (a), (b) and  $4 \text{ m s}^{-1}$  for (c), (d).

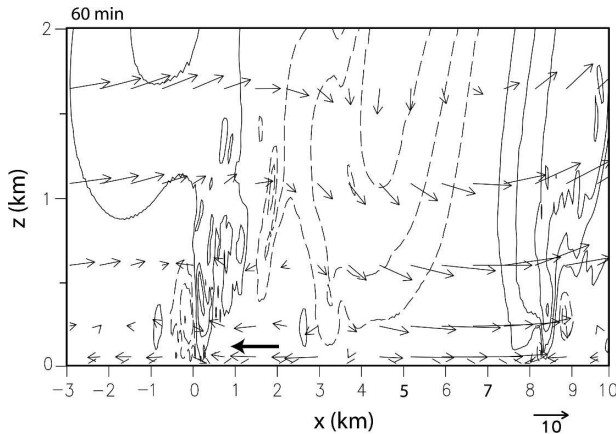


FIG. 10. Vertical cross section of vertical velocity (thin contours with  $2 \text{ m s}^{-1}$  intervals) and wind vectors for the same domain area as in Fig. 7, for the MID12.5 case. Positive (negative) values of vertical velocity are solid (dashed). Thick vector in figure indicates orientation of pressure gradient force in reversed flow region. Reference vector is given below figure.

The impact of increasing the wind speed on the deep wave mode appears to be to severely limit multicell behavior and generate stronger deep waves. Maximum vertical velocities exceed  $20 \text{ m s}^{-1}$  in the cell near  $7 \text{ km}$  at  $t = 50 \text{ min}$  and at later times. Figure 11 demonstrates that the stronger vertical motion yields greater transport of high potential temperature air from the overlying stable layer. Figure 6b shows that the higher wind speed also results in deep waves west of the hotspot, a fact that is of interest due to implications for behavior of fires well upstream of large fires in such a flow. A streamline analysis for the MID17.5 case (Figs. 9c,d) reveals that the circulations become more intense above the heating region and develop farther away from the longitude of heating sooner than in the MID12.5 case. It is straightforward to consider that for the stronger basic wind in the MID17.5 case, more energy was available for the perturbations to grow, and that outermost shear layer circulations would instigate new perturbations farther away from the hotspot more quickly than in the MID12.5 case.

#### d. Intense convective plume mode

This section considers the transition to and behavior of a stationary convective mode. The impact of a critical level in the mean flow on cellular behavior is the primary focus of this portion of the paper. Figure 12 shows Hovmöller diagrams of vertical velocity at  $z = 600 \text{ m}$  for cases LOW5, LOW7.5, and MID2.5. A dominant single cell near the hotspot remains quasi-stationary, with slowly propagating cells beyond the immediate

hotspot region for cases LOW5 and LOW7.5 (Figs. 12a,b). For the MID2.5 case, the dominant single cell exists, but there are no propagating cells as a result of the weak ambient wind. For all three cases, maximum updrafts are greater than the multicell mode and exceed  $6 \text{ m s}^{-1}$  in some cells. The reader is urged to compare Figs. 12b and 2a to appreciate the role of the critical level in the development of the intense plume mode. In the absence of a critical level (NOCL5 case, Fig. 2a), multicell plumes produced by advection develop. Only with a critical level does the slow-moving, intense fire plume mode exist. It does appear that a critical level in the basic-state flow can produce an intense fire plume, supporting the hypothesis presented at the beginning of this paper and consistent with observations of the atmosphere in the vicinity of such phenomena.

A valid question to be asked though is whether this critical level plume dependency found using the two-dimensional framework of this study could extend to a fully three-dimensional buoyant plume. A number of substantial differences between the two- and three-dimensional frameworks exist, including the character of turbulence (Tennekes and Lumley 1972), the ability of air to flow around a buoyant plume, and the presence of three-dimensional vortices able to distort the plume structure (Church et al. 1980). These limitations of a two-dimensional model motivate a comparison of the NOCL5 and LOW5 cases, rerun identically, but in a three-dimensional version of the ARPS model. The result of this comparison, presented in Fig. 13 ( $t = 60 \text{ min}$ ) and Fig. 14 ( $t = 65 \text{ min}$ ) supports the claim of critical level dependence on plume mode made in the previous paragraph. While additional three-dimensional features are noted, including the groups of updrafts and downdrafts beyond  $\pm 1\text{-km}$  radius in the  $y$  direction in the three-dimensional LOW5 case (Figs. 13a, 14a) and the bifurcation of the multicell plumes a few kilometers downstream of the hotspot in the three-dimensional NOCL5 case (Fig. 13b), two distinct plume modes can be distinguished between the fully three-dimensional cases. Therefore, findings utilizing the two-dimensional framework can safely be applied to more realistic three-dimensional plumes.

Returning to two dimensions, Figs. 15 and 16 show the vertical cross sections of vertical velocity and potential temperature for cases LOW7.5 and LOW5, respectively. The most vigorous cell in Fig. 15 (“A1”) is present near  $x = 1 \text{ km}$  at  $t = 40 \text{ min}$  and intensifies until  $t = 60 \text{ min}$  at which time the maximum vertical velocity is about  $14 \text{ m s}^{-1}$  (near  $z = 1.8 \text{ km}$ ). It is apparent from the figure that the cell nearest the hotspot generated in the LOW7.5 case is generally stationary. A slow eastward drift of about  $0.5 \text{ m s}^{-1}$  is apparent for the other

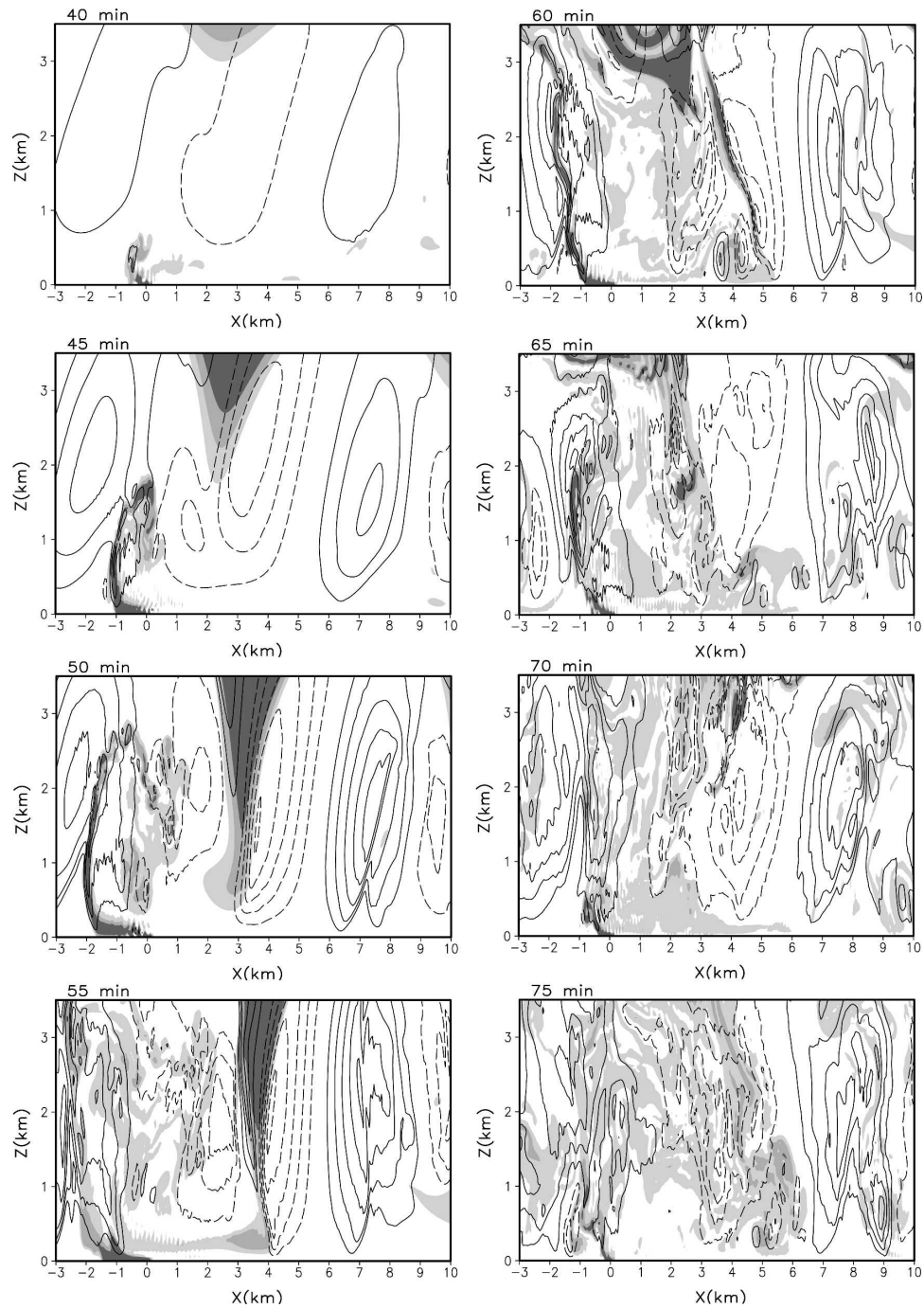


FIG. 11. As in Fig. 7 but for the MID17.5 case, with vertical velocity contoured every  $4 \text{ m s}^{-1}$ .

cells beyond  $x = 5 \text{ km}$ . A similar, though less amplified response can be seen for the LOW5 case (Fig. 16). Transport of warmer air from the stratified layer by the cells is also noted and results in a perturbed stable-neutral-layer interface.

An important aspect to discuss is the origin of the intense plume mode and the role of the critical level.

While there are cells evident both above and below the critical level in the mean flow ( $z = 1.2 \text{ km}$ ), the most intense cells are those with centroids at or just below the critical level. The exception to this is cell A1, which extends from very near the surface to about  $2 \text{ km}$ . The shear instability mechanism used to explain the deep waves in the previous section is also relevant to the

intense plume, the primary differences between the modes being the lower height of the critical level and weaker basic-state flow (and kinetic energy) in the present mode. From the streamline analysis in Fig. 17, it is apparent that horizontal vortices centered at the critical level develop as with the MID12.5 and MID17.5 cases, and that the vortex that develops nearest the hotspot is associated with the strongest cell, cell A1 (e.g., Fig. 17c). While strong vertical motion was present in the deep wave mode, one factor that distinguishes the intense plume mode from the deep wave mode is the presence of strong vertical motion near the surface, rather than a few kilometers above the surface. Also, as cell A1 is located above the hotspot, a reasonable assessment is that a combination of shear instability (i.e., the horizontal vortices) and thermal instability is important for the development of the intense plume mode.

A last feature of note is the development at about  $t = 85$  min of a second stationary cell at a position 5 km west of the hotspot in the LOW5 simulation. Figure 18 shows the vertical velocity (contoured) and streamlines for the region upstream of the hotspot, focusing on the lowest 2.5 km of the domain. Between  $t = 70$  and 90 min, a critical level vortex can be seen propagating westward in the layer above 1.5 km in sync with a region of near-surface reversed flow. While one would expect waves driven by Kelvin–Helmholtz instability to have zero phase speeds, due to the equal magnitudes of the basic horizontal wind above and below the critical level, that is,  $c = \frac{1}{2}(U_1 + U_2) \pm (i/2)(U_1 - U_2)$  [Eq. (11.51) in Kundu (1990)], where  $U_1$  and  $U_2$  are the background wind above and below the critical level, respectively, nonlinear processes yield nonzero wave phase speeds. During this time, a gradual descent of the vortex (and associated pressure minimum) occurs as a secondary cell develops near  $x = -5$  km by  $t = 80$  min. During the following 10 min, the updraft rapidly develops, reaching an intensity of greater than  $6 \text{ m s}^{-1}$  near  $z = 0.5$  km by  $t = 90$  min (Fig. 18c). During that same period, a new critical level vortex can be seen developing west of the primary updraft, which later incites new cell development (Fig. 18d) through the same process. A similar sequence of events was also active in the LOW7.5 case (see Figs. 17b–d).

A conceptual model of the updraft regeneration mechanism is presented in Fig. 19. Four stages of intense convective plume (ICP) regeneration are noted. During stage I (Fig. 19a), an initial critical level vortex develops through the shear instability process described in section 3b. The subsequent development of a region of reversed flow is indicative of boundary layer separation,

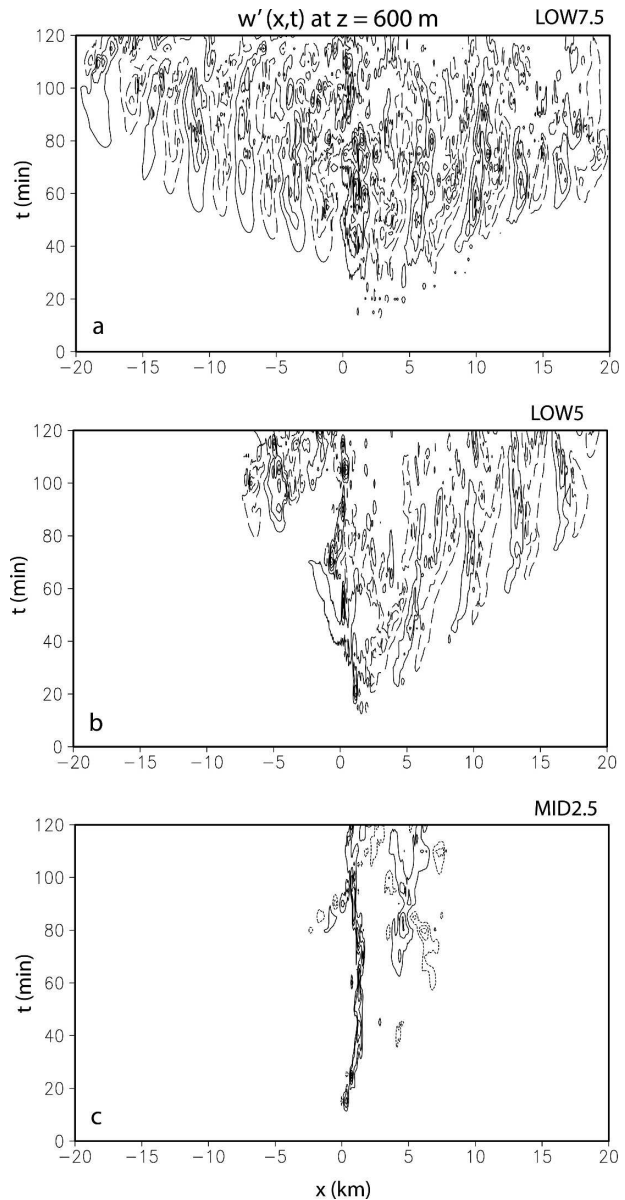


FIG. 12. As in Fig. 2 but for intense plume cases (a) LOW7.5, (b) LOW5, and (c) MID2.5.

as also discussed in section 3b. Stage II (Fig. 19b) indicates both features moving west as the area of reversed flow grows in size and the critical level vortex descends closer to the surface while growing in strength owing to the strong shear instability present at the critical level. This downward motion appears to be related to near-surface divergence below and upstream of the vortex base. Near-surface divergence below the vortex driven by acceleration of air below the lower-left quadrant of the vortex induces the vortex to gradually descend. In stage III (Fig. 19c), westward propagation and descent of the vortex continues as the vortex strength-

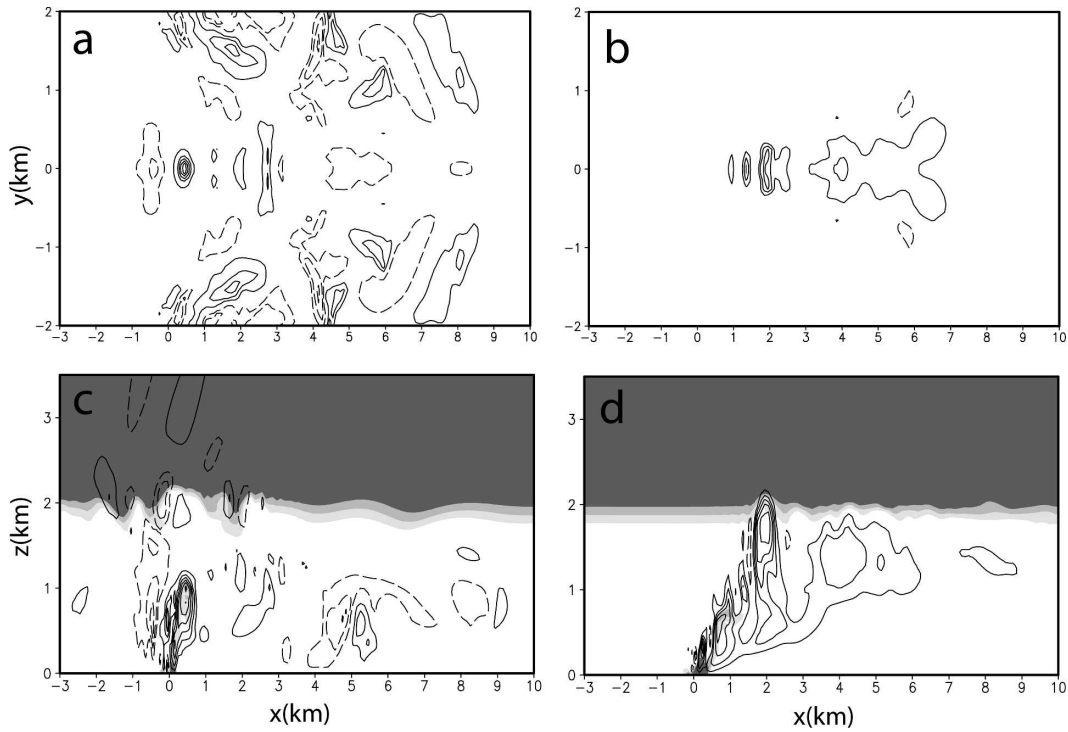


FIG. 13. (a), (b) Horizontal and (c), (d) vertical cross sections of vertical velocity for the (a), (c) LOW5 and (b), (d) NOCL5 cases rerun in a fully three-dimensional domain at  $t = 60$  min. Potential temperature is also displayed in the vertical cross sections. Contour interval and shading are same as in Fig. 7.

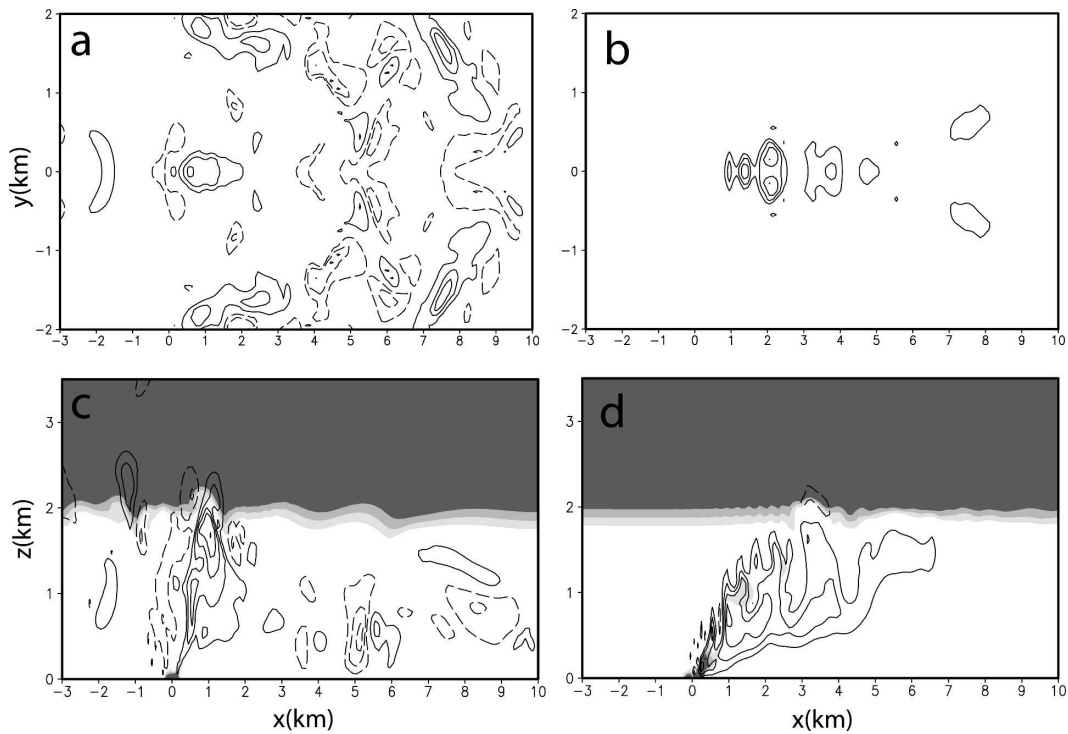


FIG. 14. As in Fig. 13 but at  $t = 65$  min.

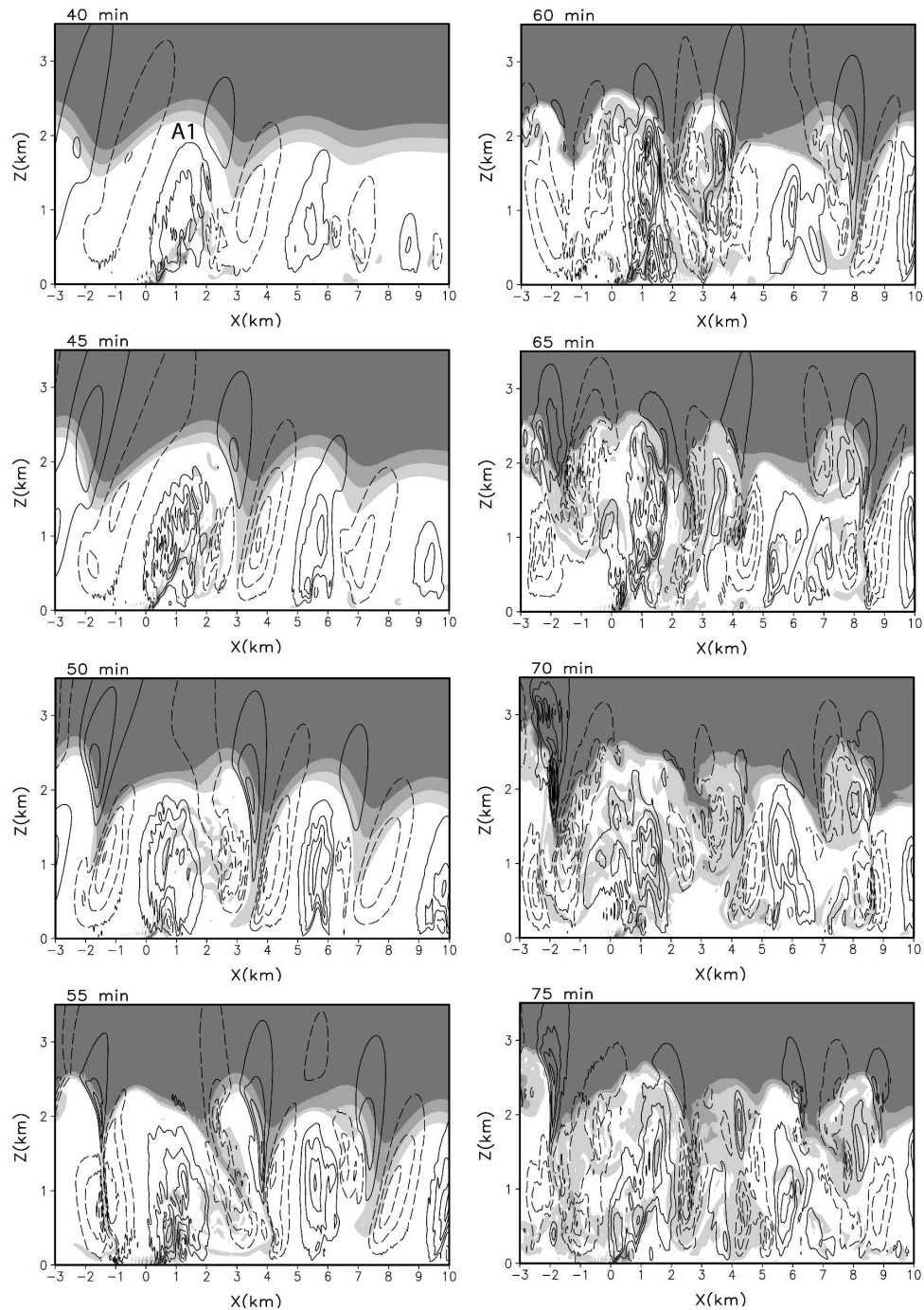


FIG. 15. As in Fig. 7 but for the LOW7.5 case. Cell A1 in first panel is discussed in the text.

ens to the point where the vertical velocities in the upward branch are of the same order as the original intense plume, and a new cell forms (ICP1). By stage IV (Fig. 19d), ICP1 enters a mature phase as the process repeats and a new vortex develops west of the original cell (ICP0).

#### *e. Sensitivity to lower boundary conditions*

As discussed in section 2a, the surface physics scheme utilized in all experiments in this study is based on bulk drag/heat transfer relations, assuming constant transfer coefficients. To examine the sensitivity of the

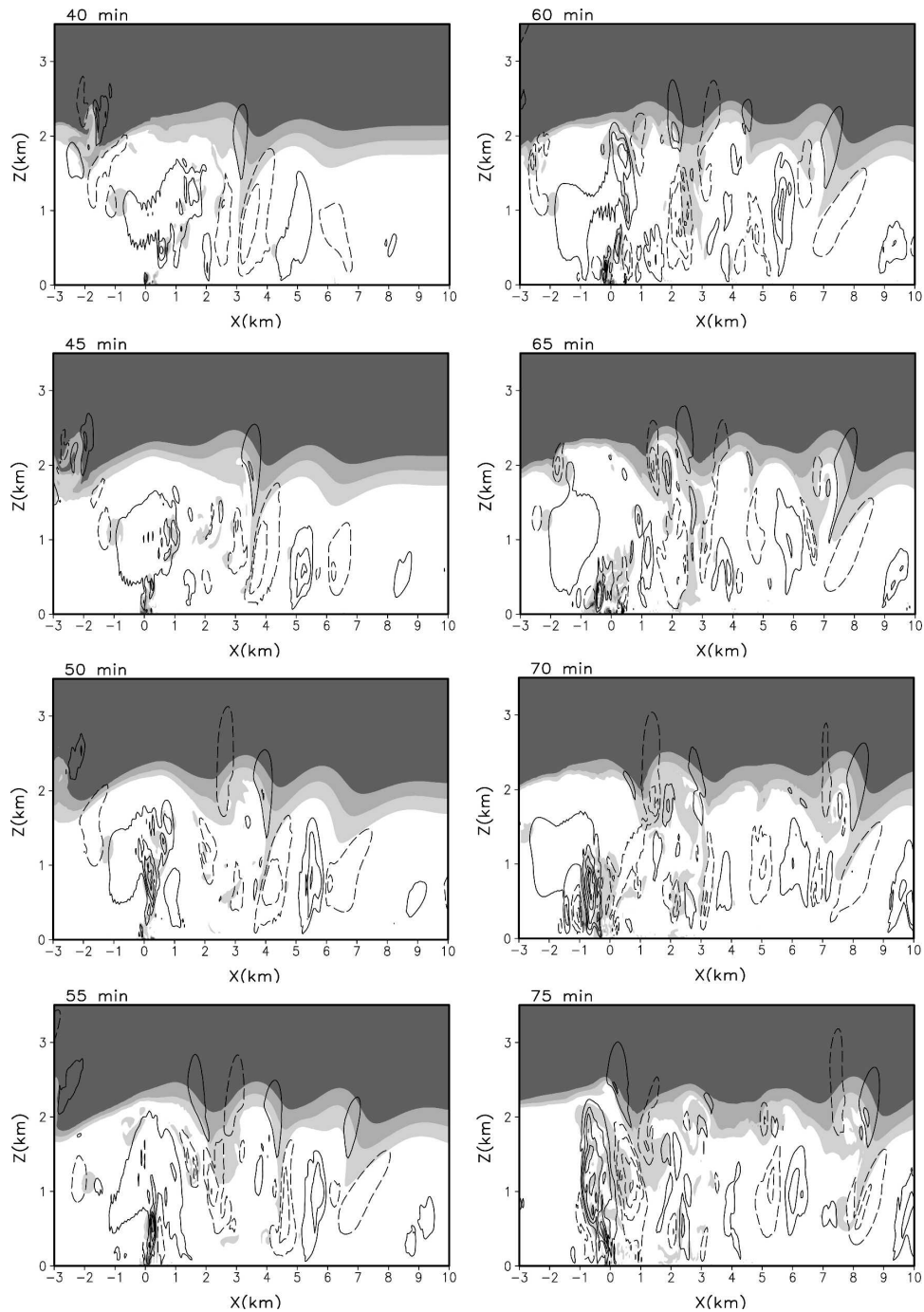


FIG. 16. As in Fig. 7 but for the LOW5 case.

results to the surface physics scheme, the MID7.5 case was rerun with coefficients calculated as a function of stability. This experiment reproduced the multicell plume mode, with the primary effect of the stronger surface heat flux being the simulation of plumes with stronger vertical velocities. This is reasonable given that the stronger heat fluxes result in a greater depth

and greater magnitude of potential temperature perturbations (not shown).

An additional experiment where the hotspot was extended 260 m farther from its original downstream end-point (but with the original surface physics scheme) yielded a similar result (Fig. 20a), as in either case air parcels are exposed to diabatic heating for a longer

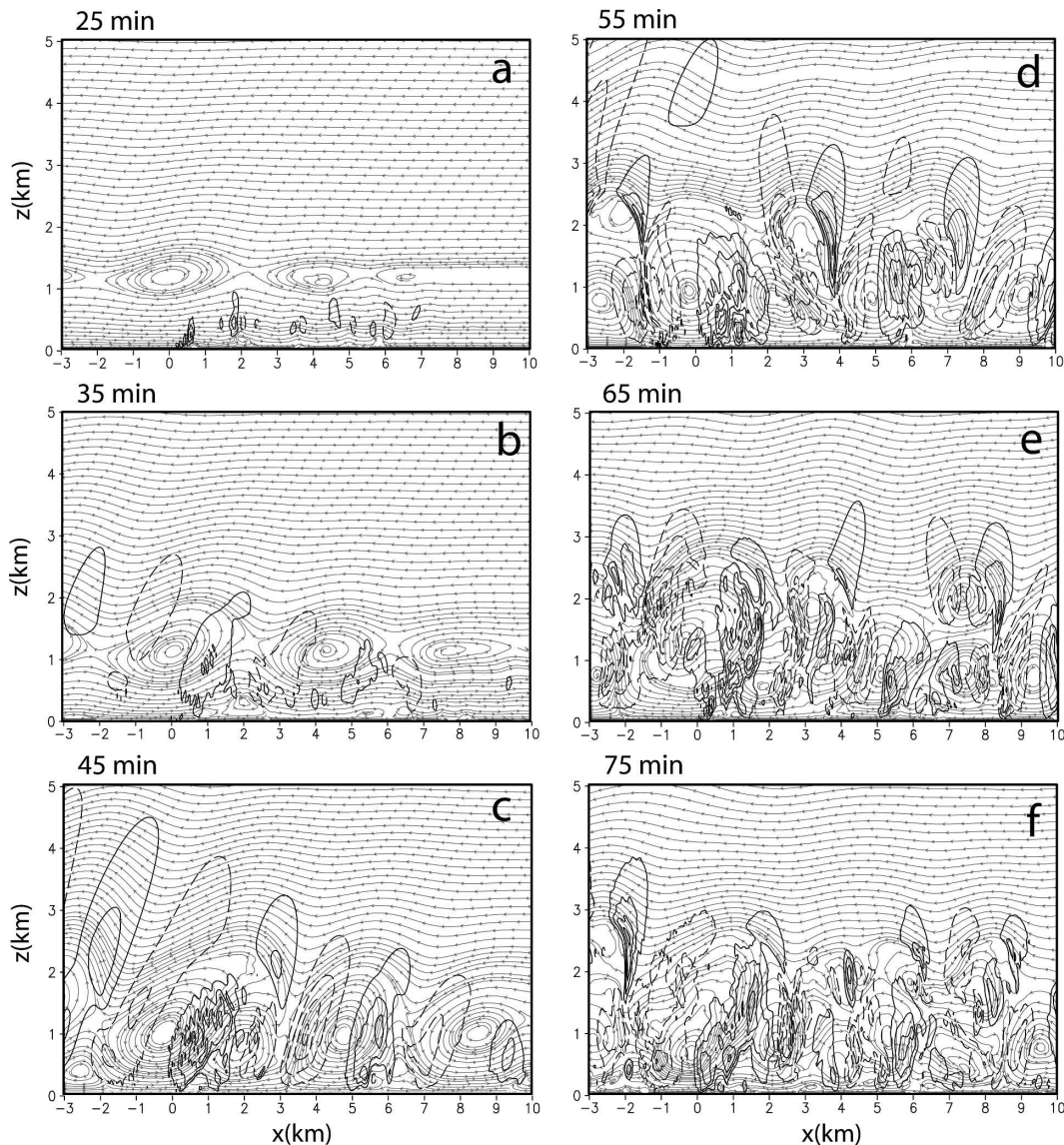


FIG. 17. As in Fig. 9a but for the LOW7.5 case with additional times included to illustrate development of intense plume mode. Only the region 3 km west to 10 km east of hotspot center is displayed.

period of time, yielding more positively buoyant cells above the hotspot. As with the MID7.5 case, the heating was extended 260 m downstream for the MID12.5 mode (Fig. 20b). Due to the strong dependence of the deep wave mode on shear instability, overall this mode shows little sensitivity to the heating structure or amplitude, other than earlier growth of the deep wave mode as the initial perturbation of the critical level by the multicell mode occurred earlier. A stronger cell west of the heating does develop when the hotspot was extended and appears to result from the easterly low-level jet seen in Fig. 10 for the original MID12.5 case experiencing sensible heat fluxes for a longer period of

time resulting in stronger low-level potential temperature perturbations and air parcels experiencing stronger buoyant upward acceleration. Comparison of the original LOW5 case with the extended hotspot version reveals mild sensitivity to the hotspot length. This is seen in a comparison of Fig. 16 at  $t = 75$  min with Fig. 20c but is more evident in a comparison of the full  $t = 40$ – $75$ -min period (not shown).

#### 4. Conclusions

The impact of varying critical level height and mean wind speed on dry convection generated above a region

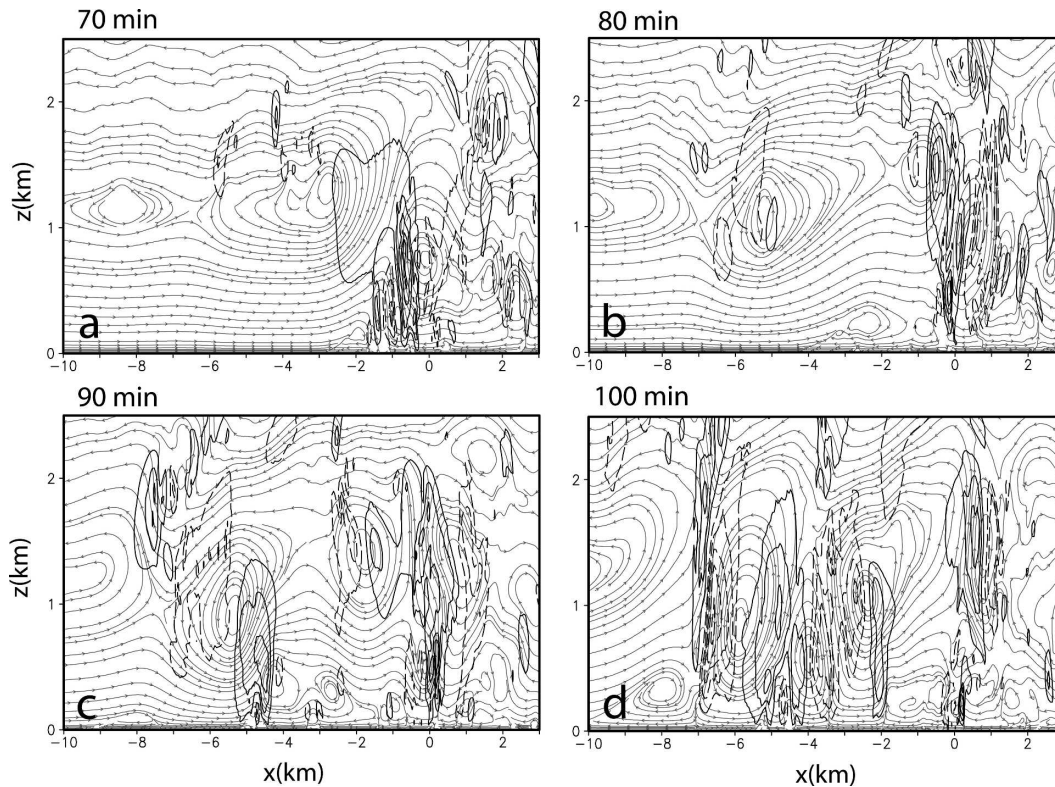


FIG. 18. As in Fig. 17 but for the LOW5 case at  $t = 70, 80, 90,$  and  $100$  min for area of domain from  $10$  km west to  $3$  km east of hotspot center and in the vertical between surface and  $2.5$  km.

of surface heating (hotspot) has been investigated. This paper discussed two sets of critical level cases, one with the critical level at  $1.2$  km (LOW) and the second at  $2.3$  km (MID). A third set of cases with a critical level at  $4.6$  km was not discussed due to a strong similarity to the MID experiment. Through variation of critical level height and mean wind speed, three distinct modes of dry convective plume, (i) multicell plume mode, (ii) deep wave mode, and (iii) intense plume mode, were simulated. The first mode was compared to multicell convection generated at gust fronts resulting from preexisting squall lines. As the base-state atmosphere in these experiments is nearly statically neutral, the multicell plumes in this study are not gravity waves, in contrast to the moist multicell phenomena. Instead, the cells in this case are akin to buoyant pulses of air or thermals that ascend and are then advected downstream by the background flow.

Analysis of Hovmöller plots of vertical velocity for the MID12.5 and MID17.5 cases revealed a second mode consisting of deep waves. The development of the deep waves in this case was noted to be due to the perturbation and unstable growth of circulations at the critical level. These deep wave modes were strong

enough to disrupt the multicell mode due to a strong easterly jet, which moved the region of multicell generation west of the hotspot after about  $1$  h of simulation time. The impact of increasing the wind speed from  $12.5$  to  $17.5$   $\text{m s}^{-1}$  was shown to strongly limit multicell growth and produce stronger deep wave modes. The development of the deep wave mode west of the hotspot in the MID17.5 case was also discussed and the difference attributed to the greater amount of basic-state energy available for the perturbations to grow and spread laterally outward away from the hotspot.

The third convective mode discussed was an intense plume that was noted to exist for the MID2.5, LOW7.5, and LOW5 cases. This mode of dry convection was distinguished by quasi-stationary motion, stronger updrafts than the multicell mode, and an apparent direct link to the thermal forcing at the hotspot. Comparison of the LOW5 case to its counterpart without a critical level (NOCL5) showed that an intense fire plume did not develop without a critical level. In the NOCL5 case, only advection-dominated multicell convection was present. These findings lend credibility to the hypothesis that the critical level plays an important role in the development of intense fire plumes.

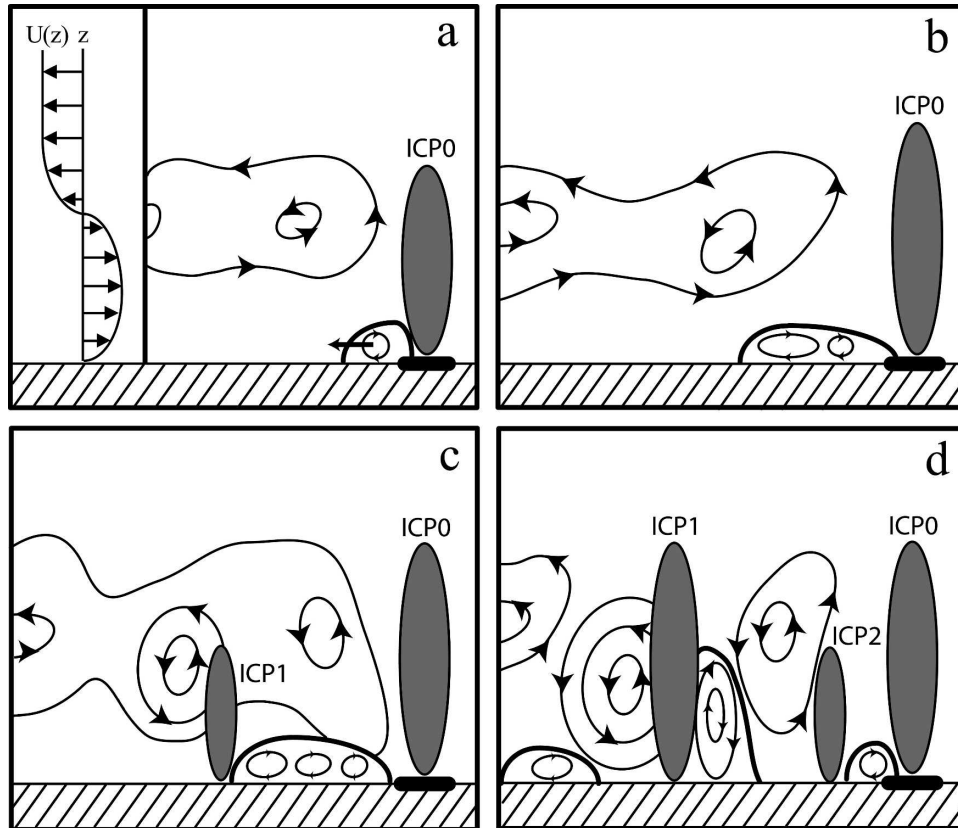


FIG. 19. Conceptual model of ICP regeneration mechanism. Four stages are found for ICP regeneration: (a) stage I: an initial critical level vortex develops through shear instability while a region of near-surface reversed flow, indicative of boundary layer separation, simultaneously develops. (b) Stage II: both features move west as the area of reversed flow grows in size and the critical level vortex descends closer to the surface while growing in strength owing to the strong shear instability present at the critical level. (c) Stage III: westward propagation and descent of the vortex continues as the vortex strengthens. At this stage, vertical velocities in the upward branch are of the same order as the original intense plume, signaling development of the new cell (ICP1). (d) Stage IV: ICP1 enters a mature phase as the process repeats and a new vortex (ICP2) develops west of the original cell (ICP0).

An extension of this analysis to three dimensions supported the two-dimensional findings. The critical level role in the intense plume mode development was noted to be similar to that for the deep wave modes, except that the horizontal vortices at the critical level are located closer to the surface for the intense plume mode, where a juxtaposition of the plumes generated by the thermal instability above the hotspot and the critical level vortices promote strong updrafts near the surface.

An interesting aspect of the intense plume mode was a new cell development 5 km west of the hotspot at about 80 min into the LOW5 simulation. The new cell was noted to form in the upward vertical branch of the critical level vortex growing in strength immediately west of the original intense plume. Near-surface divergence below the vortex, driven by acceleration of the

flow below the lower-left quadrant of the vortex, is consistent with the descent of the vortex during the period of time covered by the conceptual model, as well as the growth of the new cell near 600 m above ground level. Similar behavior was also found for the LOW7.5 case.

Future experiments will include environmental moisture as well as a simple parameterization of the contribution of water vapor from combustion and evaporation of fuel moisture in these two- and three-dimensional experiments, to investigate if these dry convective modes can also be realized in a moist convective setting. Additional work will also include multidirectional shear so as to evaluate the role of such shear in plume development. Through the work done to this point and the important future work to be accomplished, it is hoped that a better understanding of

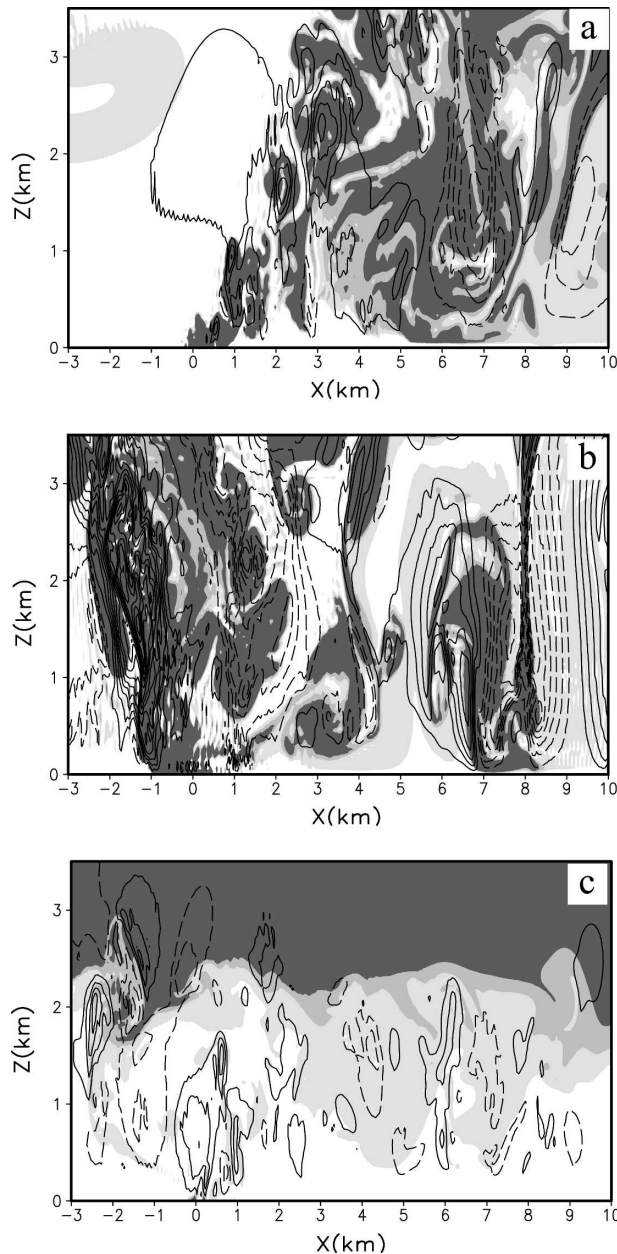


FIG. 20. As in Fig. 3 for (a) MID7.5, (b) MID12.5, and (c) LOW5 cases at  $t = 75$  min, except with hotspot extended 260 m farther downstream (east) of the hotspot used in the original experiments. Potential temperature is shaded in (a) as in Fig. 3, where shading is same as in Fig. 7.

the different plume modes present in the vicinity of forest fires will be achieved.

**Acknowledgments.** This research was supported by the USDA Forest Service Research Joint Venture Agreement 02-JV-11231300-051. We wish to thank the three anonymous reviewers of this manuscript for their comments and suggestions.

## REFERENCES

- Banta, R. M., L. D. Olivier, E. T. Holloway, R. A. Kropfli, B. W. Bartram, R. E. Cupp, and M. J. Post, 1992: Smoke-column observations from two forest fires using Doppler lidar and Doppler radar. *J. Appl. Meteor.*, **31**, 1328–1349.
- Byram, G. M., 1966: Scaling laws for modeling mass fires. *Pyrodynamics*, **4**, 271–284.
- Church, C. R., J. T. Snow, and J. Dessens, 1980: Intense atmospheric vortices associated with a 1000 MW fire. *Bull. Amer. Meteor. Soc.*, **61**, 682–694.
- Clark, T. L., M. A. Jenkins, J. L. Coen, and D. R. Packham, 1996: A coupled atmosphere-fire model: Role of the convective Froude number and dynamic fingering at the fireline. *Int. J. Wildland Fire*, **6**, 177–190.
- Cunningham, P., S. A. Ferguson, T. J. Brown, S. L. Goodrick, M. Flannigan, M. Y. Hussaini, and R. R. Linn, 2005: Coherent vortical structures in numerical simulations of buoyant plumes from wildland fires. *Int. J. Wildland Fire*, **14**, 61–75.
- Fovell, R. G., and P. S. Dailey, 1995: The temporal behavior of numerically simulated multicell-type storms. Part I: Modes of behavior. *J. Atmos. Sci.*, **52**, 2073–2095.
- , and P.-H. Tan, 1998: The temporal behavior of numerically simulated multicell-type storms. Part II: The convective cell life cycle and cell regeneration. *Mon. Wea. Rev.*, **126**, 551–577.
- Grishin, A. M., A. D. Gruzin, and É. É. Gruzina, 1984: Aerodynamics and heat exchange between the front of a forest fire and the surface layer of the atmosphere. *J. Appl. Mech. Tech. Phys.*, **25**, 889–894.
- Jenkins, M. A., T. Clark, and J. Coen, 2001: Coupling atmospheric and fire models. *Forest Fires: Behavior and Ecological Effects*, E. A. Johnson and K. Miyanishi, Eds., Academic Press, 257–302.
- Kundu, P. K., 1990: *Fluid Mechanics*. Academic Press, 638 pp.
- LeBlond, P. H., and L. A. Mysak, 1978: *Waves in the Ocean*. Elsevier Scientific, 602 pp.
- Lin, Y.-L., and H.-Y. Chun, 1993: Structures of dynamically unstable shear flows and their implications for shallow internal gravity waves. *Meteor. Atmos. Phys.*, **52**, 59–68.
- , and L. E. Joyce, 2001: A further study of the mechanisms of cell regeneration, propagation, and development within two-dimensional multicell storms. *J. Atmos. Sci.*, **58**, 2957–2988.
- , T.-A. Wang, and R. P. Weglarz, 1993: Interactions between gravity waves and cold air outflows in a stably stratified uniform flow. *J. Atmos. Sci.*, **50**, 3790–3816.
- , R. L. Deal, and M. S. Kulie, 1998: Mechanisms of cell regeneration, development, and propagation within a two-dimensional multicell storm. *J. Atmos. Sci.*, **55**, 1867–1886.
- Lindzen, R. S., and A. J. Rosenthal, 1983: Instabilities in a stratified fluid having one critical level. Part III: Kelvin-Helmholtz instabilities as overreflected waves. *J. Atmos. Sci.*, **40**, 530–542.
- McRae, D. J., and B. J. Stocks, 1987: Large-scale convection burning in Ontario. *Proc. Ninth Conf. on Fire and Forest Meteorology*, San Diego, CA, Amer. Meteor. Soc., 23–30.
- , and M. D. Flannigan, 1990: Development of large vortices on prescribed fires. *Can. J. For. Res.*, **20**, 1878–1887.
- Raphael, M. N., 2003: The Santa Ana winds of California. *Earth Interactions*, **7**. [Available online at <http://EarthInteractions.org>.]
- Raymond, D. J., and R. Rotunno, 1989: Response of a stably stratified flow to cooling. *J. Atmos. Sci.*, **46**, 2830–2837.

- Redelsperger, J.-L., and T. L. Clark, 1990: The initiation and horizontal scale selection of convection over gently sloping terrain. *J. Atmos. Sci.*, **47**, 516–541.
- Simard, A. J., D. A. Haines, R. W. Blank, and J. S. Frost, 1983: The Mack Lake fire. USDA Forest Service Gen. Tech. Rep. NC-83, 38 pp. [Available online at [http://www.ncrs.fs.fed.us/pubs/gtr/gtr\\_nc083.pdf](http://www.ncrs.fs.fed.us/pubs/gtr/gtr_nc083.pdf).]
- Stull, R. B., 1988: *An Introduction to Boundary Layer Meteorology*. Kluwer Academic, 666 pp.
- Tennekes, H., and J. L. Lumley, 1972: *A First Course in Turbulence*. MIT Press, 300 pp.
- Werth, P., and R. Ochoa, 1993: The evaluation of Idaho wildfire growth using the Haines index. *Wea. Forecasting*, **8**, 223–234.
- Xue, M., K. K. Droegemeier, and V. Wong, 2000: The Advanced Regional Prediction System (ARPS)—A multi-scale non-hydrostatic atmospheric simulation and prediction model. Part I: Model dynamics and verification. *Meteor. Atmos. Phys.*, **75**, 161–193.
- , and Coauthors, 2001: The Advanced Regional Prediction System (ARPS)—A multi-scale nonhydrostatic atmospheric simulation and prediction tool. Part II: Model physics and applications. *Meteor. Atmos. Phys.*, **76**, 143–165.
- , D. Wang, J. Gao, K. Brewster, and K. K. Droegemeier, 2003: The Advanced Regional Prediction System (ARPS), storm-scale numerical weather prediction and data assimilation. *Meteor. Atmos. Phys.*, **82**, 139–170.
- Yang, M.-J., and R. A. Houze Jr., 1995: Multicell squall-line structure as a manifestation of vertically trapped gravity waves. *Mon. Wea. Rev.*, **123**, 641–661.

Copyright of *Journal of the Atmospheric Sciences* is the property of *American Meteorological Society* and its content may not be copied or emailed to multiple sites or posted to a listserv without the copyright holder's express written permission. However, users may print, download, or email articles for individual use.